



**HAL**  
open science

# Nonlinear effect of grain elongation on the flow rate in silo discharge

Agathe Bignon, Mathieu Renouf, Roland Sicard, Emilien Azéma

► **To cite this version:**

Agathe Bignon, Mathieu Renouf, Roland Sicard, Emilien Azéma. Nonlinear effect of grain elongation on the flow rate in silo discharge. *Physical Review E*, 2023, 108 (5), pp.054901. 10.1103/PhysRevE.108.054901 . hal-04273446

**HAL Id: hal-04273446**

**<https://hal.science/hal-04273446v1>**

Submitted on 7 Nov 2023

**HAL** is a multi-disciplinary open access archive for the deposit and dissemination of scientific research documents, whether they are published or not. The documents may come from teaching and research institutions in France or abroad, or from public or private research centers.

L'archive ouverte pluridisciplinaire **HAL**, est destinée au dépôt et à la diffusion de documents scientifiques de niveau recherche, publiés ou non, émanant des établissements d'enseignement et de recherche français ou étrangers, des laboratoires publics ou privés.

**Nonlinear effect of grain elongation on the flow rate in silo discharge**Agathe Bignon<sup>1,2,\*</sup>, Mathieu Renouf<sup>1,†</sup>, Roland Sicard<sup>2,‡</sup> and Emilien Azéma<sup>1,3,§</sup><sup>1</sup>*LMGC, Université de Montpellier, CNRS, 34090 Montpellier, Herault, France*<sup>2</sup>*Thess Corporate, 34090 Montpellier, Herault, France*<sup>3</sup>*Institut Universitaire de France (IUF), 75231 Paris, France*

(Received 19 April 2023; accepted 6 October 2023; published 1 November 2023)

By means of two-dimensional numerical simulations based on contact dynamics, we present a systematic analysis of the joint effects of grain shape (i.e., grain elongation) and system size on silo discharge for increasing orifice sizes  $D$ . Grains are rounded-cap rectangles whose aspect ratio are varied from 1 (disks) to 7. In order to clearly isolate the effect of grain shape, the mass of the grains is keeping constant as well as the condition of the discharge by reintroducing the exiting grains at the top of the silo. In order to quantify the possible size effects, the thickness  $W$  of the silos is varied from 7 to 70 grains diameter, while keeping the silos aspect ratio always equal to 2. We find that, as long as size effects are negligible, the flow rate  $Q$  increases as a Beverloo-like function with  $D$ , also for the most elongated grains. In contrast, the effects of grain elongation on the flow rate depend on orifice size. For small normalized orifice sizes, the flow rate is nearly independent with grain elongation. For intermediate normalized orifice sizes the flow rate first increases with grain elongation up to a maximum value that depends on the normalized size of the orifice and saturates as the grains become more elongated. For larger normalized orifice size, the flow rate is an increasing function of grains' aspect ratio. Velocity profiles and packing fraction profiles close to the orifice turn out to be self-similar for all grain shapes and for the whole range of orifice and system sizes studied. Following the methodology introduced by Janda *et al.* [*Phys. Rev. Lett.* **108**, 248001 (2012)], we explain the nonlinear variation of  $Q$  with grain elongation, and for all orifice sizes, from compensation mechanisms between the velocity and packing fraction measured at the center of the orifice. Finally, an equation to predict the evolution of  $Q$  as a function of the aspect ratio of the grains is deduced.

DOI: [10.1103/PhysRevE.108.054901](https://doi.org/10.1103/PhysRevE.108.054901)**I. INTRODUCTION**

From the measurement of time in an hourglass [1] to the storage and discharge of huge quantities of grains in different industrial contexts [2–4], the flow of grains within a silo has been and still is the subject of a large number of studies. Generally speaking, in a grain column, the stress measured at the bottom does not increase linearly with the filling height but quickly saturates at a maximum value. The independence of the stress explains the well-known fact that, unlike liquids, the flow rate  $Q$  of the grains is constant. This effect has sometimes been attributed to the presence of force chains, arguing that the arches “support” the weight of the upper layers of grains. But Janssen’s model [5] and its experimental verification [6] indicate that the physical origin of stress saturation is the mobilization of the frictional force at the walls.

Nevertheless, there are effects that cannot be explained by macroscopic arguments of this type. For example, the flow in a silo is continuous only when the diameter  $D$  of the orifice is larger than a critical diameter [7]. In this case, using dimensional analysis (assuming a free fall of the grains under gravity  $g$  above the orifice [8]), it can be shown that the discharge

rate is of the order of  $Q \sim g^{1/2} D^{n+1/2}$ , where  $n$  is 1 in two dimensions and 2 in three.

Otherwise, if the orifice size is a few times larger than the grains size  $d$ , metastable regimes not captured by the dimensional analysis exist, revealing intermittent flows that are related both to the discrete nature of the medium and to the presence of grain arches above the orifice [9]. Avalanche statistics (defined from the number of grains flowing through the orifice from two metastable regimes) reveals that the probability density of avalanche size is a decreasing exponential function independent of the orifice size. In contrast, the mean avalanche size increases and diverges as a critical aperture is approached [10]. Note that a number of technological strategies have been imagined to avoid clogging for small apertures [11–14].

From these observations, the first semiempirical equation was developed by Beverloo [8] in the form  $Q = C \rho_g \sqrt{g} (D - \kappa d)^{n+1/2}$ , where  $\rho_g$  denotes the bulk density of grains, and  $C$  and  $\kappa$  are material-dependent parameters. The parameter  $\kappa$  was introduced in order to take into account a reduced orifice diameter induced by finite-size effects. Although the fitting parameters are not well defined physically, several numerical and experimental studies, mainly based on circular or spherical grains [15], have proven that the Beverloo’s law is robust for large orifice, but is failing for small orifices where clogging prevails [16].

As far as we know, the first theoretical expression of the flow rate is attributed to Janda *et al.* [17]. This was derived

\* [agathe.bignon@umontpellier.fr](mailto:agathe.bignon@umontpellier.fr)† [mathieu.renouf@umontpellier.fr](mailto:mathieu.renouf@umontpellier.fr)‡ [rsicard@thess-corp.fr](mailto:rsicard@thess-corp.fr)§ [emilien.azema@umontpellier.fr](mailto:emilien.azema@umontpellier.fr)

on the basis of clear physical parameters that relied on the self-similar properties of velocity and packing fraction profiles close to the orifice. Using 2D experiments with circular grains, they show that finite-size effects for small orifices do not have to be taken into account via the *ad hoc* parameters  $\kappa d$ , but rather via the variations of the solid fraction close to the orifice, as a function of the orifice size. This idea was also suggested in the work of Mankok [18]. Very recently, Benyamine *et al.* [19] as well as Zhou *et al.* [20] have extended the “Janda” model to the flow of bidispersed disks and spheres.

While most existing work on silo discharge has been carried out using model materials (i.e., disks or spheres), grains encountered in nature and industry are rarely spherical. Moreover, it is now well reported in the literature that the qualitative and often nontrivial behavior induced by particle shape, such as the nonlinear dependency on strength with packing fraction as the shape deviates from circular or spherical shape [21–24], or the role of side-side (in two dimensions) or face-face (in three) contacts on stress transmission and fabric properties in sheared granular systems [23,25–27]. Thus, we can also expect nontrivial effects induced by particle shapes in a silo geometry.

For example, recent works have shown that the probability of clogging increases with grains angularity [10] or with grains’ elongation [28]. More disconcerting, seemingly contradictory results were obtained with elongated grains, where the flow rate may increase [28,29] or decrease [30–32] as the grain elongation increases. Even more surprising, the flow rate may be independent with grain elongations in frictionless 3D systems [29]. Moreover, in a narrow silo the discharge of elongated grains is time dependent, which is not the case for spherical grains, suggesting that size effects may dominate with nonspherical particles [33]. The origins of the discrepancy of all these results are not well understood, and in more general terms it is unclear whether, and how, current flow models can be extended to nonspherical particles.

The objective of this paper is to investigate in more detail the combined effects of grain elongation and system size on the silo discharge of 2D rigid grain assemblies by using a discrete element method: contact dynamics (CD). The particles considered are rectangles with rounded end caps that we call “rounded-cap rectangles” (RCRs), with aspect ratios ranging from 1 (disks) to 7. The thickness of the silos varies from 7 to 70 grain diameters, keeping the aspect ratio of the silos constant and equal to 2 in order to quantify possible size effects. Finally, in order to clearly isolate the effect of grain shape, the mass of the grains is kept constant as well as the discharge condition by reintroducing the outgoing grains at the top of the silo. In this way, the only parameters that change in our simulations are the shape of the grains and the size of the systems.

The paper is structured as follows. In Sec. II we briefly describe the numerical method used in the simulations, the sample constructions, and the procedure followed to break the arches and reintroduce the grains. Section III is devoted to the analysis of the flow rate as a function of system size and grain shapes. In Sec. IV we analyze the different velocity and solid fraction profiles close to the orifice, as a function of the system parameters. Inspired by the work of Janda *et al.* [17]

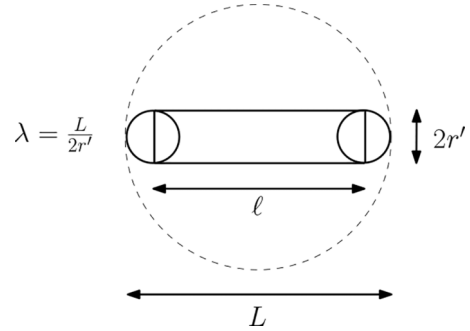


FIG. 1. Geometry of a rounded-cap-rectangle (RCR) grain.

we will derive a model to predict the flow as a function of grain elongation.

We conclude with a summary of the main findings of this work in Sec. V.

## II. MODEL DESCRIPTION

### A. Numerical method

For the simulations we use contact dynamics (CD), developed by Moreau and Jean, a nonsmooth discrete element method (DEM) [34,35]. This method is based on an implicit time integration of the equations of motion and a nonsmooth formulation of the contact and dry friction between the grains. No regularization is made in the calculation of the contact forces, and the impacts are considered perfectly plastic (zero restitution). At each time step, an iterative, nonlinear (parallelized [36]) Gauss-Seidel type solution algorithm is used to determine the set of contact forces. Due to the unconditionally stable character of this method, it is particularly well suited to simulate large assemblies of frictional grains of any shape.

As shown in Fig. 1, each elongated grain is modeled as a rectangle of length  $\ell$  and width  $2r'$ , whose rounded end caps are represented by two juxtaposed disks of radius  $r$ . In what follows, we will call this grain a “rounded end-cap rectangle” (RCR) [22]. The elongation of an RCR grain is given by the aspect ratio  $\lambda = (\ell + 2r')/(2r') = L/(2r')$ , where  $L = \ell + 2r'$  is the length of an RCR grain. An aspect ratio of 1 corresponds to a circle of diameter  $d = 2r'$  (i.e.,  $\ell = 0$ ).

Basically, in RCR grain assembly three kinds of geometrical contact may arise: side-side [Fig. 2(a)], which are linear contacts, or cap-cap [Fig. 2(b)] or cap-side [Fig. 2(c)], which are “punctual” contacts. Since an RCR grain is built as a “cluster” of three rigid particles, the contacts are detected separately between disk-disk or disk-polygon particles, each of them involving a single point of contact. By construction, linear contacts involve necessarily two disk-polygon contacts and thus are treated by two contact points, as typically done

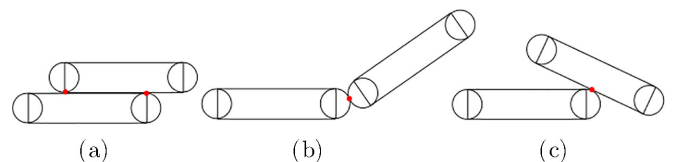


FIG. 2. Contact configurations in RCR grain assemblies.

in the CD method. Thus, two forces are calculated by the CD algorithm, but only their resultant and application points are material. The procedure and implementation for the treatment of linear contact in the framework of the CD method are described in detail in Ref. [37]. We used the platform LMGC90, which is a multipurpose software developed in Montpellier, capable of modeling a collection of deformable or undeformable particles of various shapes [38,39].

### B. Sample preparation and dimensionless parameters

We consider 2D silos of rectangular shape of width  $W$  and height  $H = 2W$  with a varying size  $D$  of the orifice.

$N_g$  randomly oriented grains of length  $L$  are mechanically deposited within the silo under the action of the gravity. The friction between grains, and with the walls, is fixed to 0.4. In order to isolate the effect of grain shape, in all the simulations presented below, both the area Eq. 1(a) and the mass Eq. 1(b) of one elongated grain of aspect ratio  $\lambda$  are kept equal to that of disk of diameter  $d$ . Keeping mass and area constant is in our case not the same thing since the RCR grain is numerically built from two disks. Indeed, this translates into these two set of equations:

$$\mathcal{A}_d(d) = \mathcal{A}_d(2r') + \mathcal{A}_r(\ell, 2r'), \quad (a)$$

$$\rho_d \mathcal{A}_d(d) = \rho_r [2\mathcal{A}_d(2r') + \mathcal{A}_r(\ell, 2r')], \quad (b) \quad (1)$$

where  $\mathcal{A}_d$  is the area of a disk of diameter  $2r'$ , or  $d$ , and  $\mathcal{A}_r(\ell, r')$  is the area of a rectangle of length  $\ell$  and thickness  $2r'$ .  $\rho_r, \rho_d$  refer to the density of the RCR for  $\lambda > 1$ ,  $\lambda = 1$ , respectively. Note that  $\mathcal{A}_d(2r')$  is counted two times in the left-hand expression in Eq. 1(b) to consider the numerical construction of the RCR. Then, following simple algebra, we get  $L = \lambda d \sqrt{\pi/[\pi + 2\lambda - 2]}$  and  $\rho_r = \rho_d(\pi + 2\lambda - 2)/\pi$ , which allow us to build the corresponding RCR grain knowing the aspect ratio  $\lambda$  and the diameter  $d$ . For all systems that will be simulated, a weak size polydispersity is considered by varying the diameter  $d$  between  $d_{\min} = 0.8\langle d \rangle$  and  $d_{\max} = 1.2\langle d \rangle$ , with a uniform distribution of the grain area fractions, and  $\langle d \rangle$  the mean diameter.

The width of a silo is quantified as a function of the diameter  $\bar{d} \equiv L$  of the circumscribed circle of the RCR grain by  $W = \xi \bar{d}$ , with  $\xi$  the parameter measuring the size of the silo with respect to grain diameter. In addition to the dimensionless parameters  $\xi$  and  $\lambda$ , we also consider the normalized orifice size by  $\alpha = D/\bar{d}$ . Thus, by combining  $\xi$  and  $\alpha$ , we can also build the dimensionless number  $\eta = \xi/\alpha = W/D$  as the ratio between the width of the silo and the size of the orifice. As far as we know, this dimensionless number is often referred to in the experimental work of Nedderman [40] and Brown [41], who show that size effects in sphere assemblies disappear if  $\eta \gtrsim 2.5$ . The main notations are summarized in Table I.

### C. “Perpetual” flow in a silo and parametric study

As also done in [42], in order to keep the discharge conditions constant under the action of gravity  $g$ , the grains falling through the orifice are reintroduced into the top of the silo with zero velocity and random orientation, as illustrated in Fig. 3. Thus, the total number of grains remains constant during the

TABLE I. Parameter summary.

Parameter	Formula
Silo width and height	$W, H = 2W$
Orifice size	$D$
Diameter of disks	$d$
RCR thickness and length	$2r', L$
Circumscribing diameter of RCR	$\bar{d} \equiv L$
Grain elongation ratio	$\lambda = L/(2r')$
Silo width to grain length ratio	$\xi = W/\bar{d}$
Aperture width to grain length ratio	$\alpha = D/\bar{d}$
Silo width to aperture ratio	$\eta = W/D$

discharge. The difficulty is then to remove an arch when a clog appears to continue the flow. In practice, an arch can be considered stable only when all particles are at rest. Otherwise, a metastable arch located just above the orifice can exist and can be destabilized only by the movement of other grains. Thus, in practice we will assume that if the normalized mean kinetic energy  $\langle E_c^g/E_0 \rangle_{N_p}$ , where  $E_0 = 0.5m\langle d \rangle/g$  the typical free-fall kinetic energy, is below 0.005, during a normalized time  $t/t_0 = 25$ , where  $t_0 = \sqrt{d/g}$ , then the flow is stopped. In order to restart the flow, the arch obstructing the orifice is destabilized by removing the grain closest to the center of the orifice and reintroducing it at the top of the silo. This grain will be treated as a “passing grain” (grain leaving the silo). This simple procedure is always enough to restart the flow.

In this work, we aim to quantify the effects of the geometrical parameters ( $\lambda, \xi, \alpha, \eta$ ) defined previously on the flow rate  $Q$ . Thus, we performed several sets of simulations, changing one parameter each time while all the other parameters are maintained constant. In order to analyze the effect of system width with respect to the mean grain size, the  $\xi$  parameter is varying in the range [7,15,22,44,70], and to analyze the effect

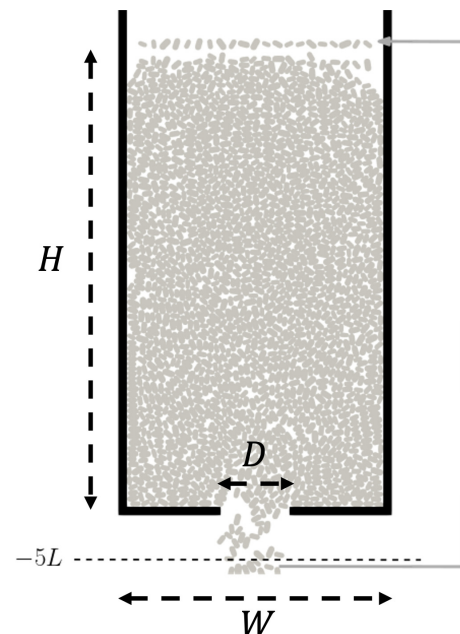


FIG. 3. Illustration of the recirculation mechanism, for  $\lambda = 2$  and  $\xi = 22$ .

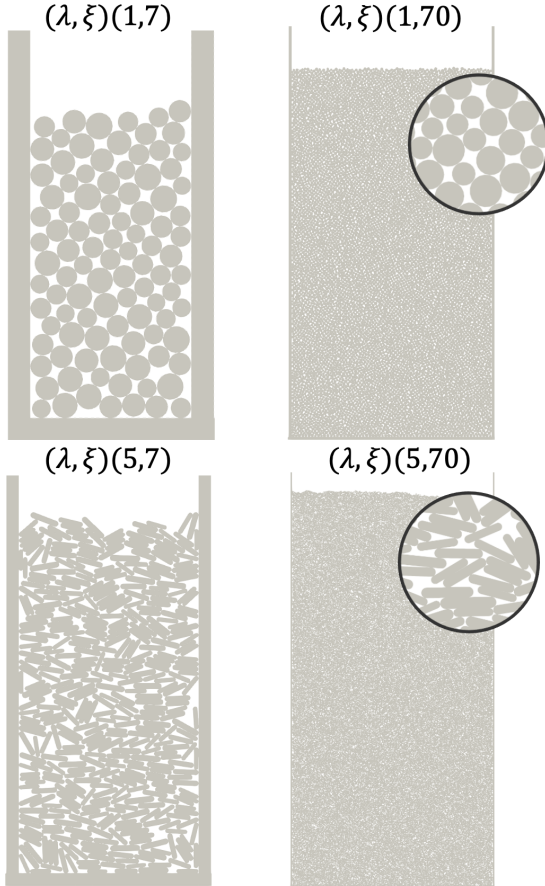


FIG. 4. Examples of the generated packings at the initial state for extremal values of  $\xi$  and  $\lambda = [1, 5]$ . The insets show a grain-scale views of the packings.

of system width with respect to orifice size, the  $\eta$ -parameter is varied between 1 to 15, and finally, to analyze the effect of grain elongation, the  $\lambda$  parameter is varied in the range [1,2,3,4,5,6,7].

Although the number  $N_g$  of grain remains constant for a fixed couple  $(\lambda, \xi)$ , it increases from 100 for  $(\lambda, \xi) = (1, 7)$  to 10 000 for  $(\lambda, \xi) = (1, 70)$ , and from 417 for  $(\lambda, \xi) = (5, 7)$  to 41 037 for  $(\lambda, \xi) = (5, 70)$ . Figure 4 displays snapshots of the silo for the extreme values of  $\xi$  and  $\lambda = [1, 5]$ .

Finally, it is important to note that to have “good” statistics in terms of a clogging event, typical packing fraction, or velocity close to the orifice, very long simulations are needed so that the standard deviations measured around the mean values do not change by adding new data. For example, the total time of simulation goes from  $40\,000t_0$  for  $(\lambda, \xi) = (1, 7)$  to  $8000t_0$  for  $(\lambda, \xi) = (1, 70)$ . For elongated grains it goes from  $2200t_0$  for  $(\lambda, \xi) = (5, 7)$  to  $1500t_0$  for  $(\lambda, \xi) = (5, 70)$ . A total of 150 simulations were performed for different values of  $(\lambda, \xi, \alpha, \eta)$

### III. FLOW RATE

#### A. Flow description (main features)

The flow rate is measured by considering the time series of the cumulative number  $N(t)$  of grains passing through the

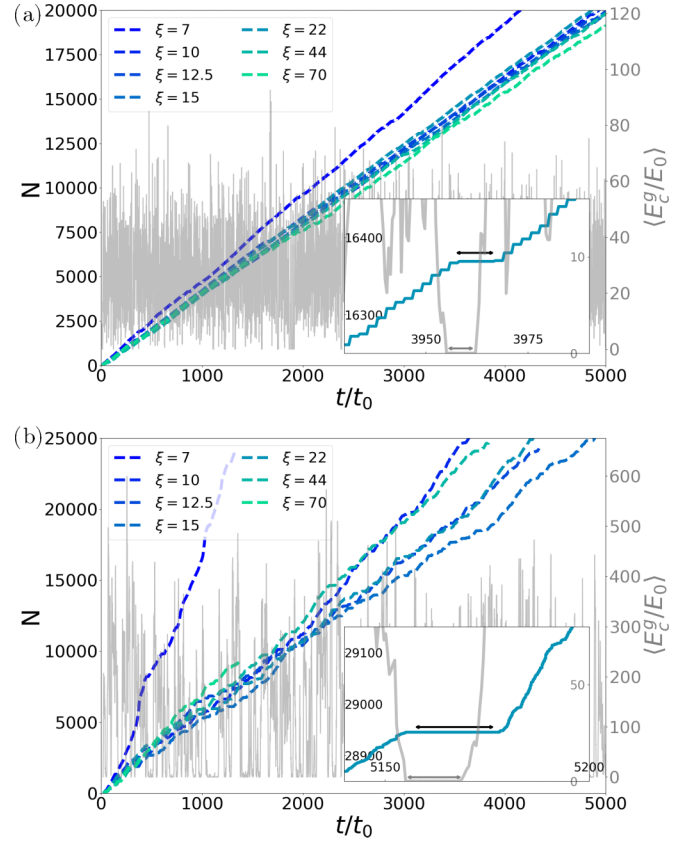


FIG. 5. Number of grain discharge (left and black y axis) and normalized kinetic energy (only for  $\xi = 22$ ; right and gray y axis) as a function of  $t/t_0$  for  $(\lambda, \xi, D/\bar{d}) = (1, [15, 22], 4.9)$  (a) and  $(\lambda, \xi, D/\bar{d}) = (5, [15, 22], 4.9)$  (b); inset shows a zoom of the data only for  $\xi = 22$ .

orifice, as illustrated in Fig. 5 for  $\lambda = 1$  and  $\lambda = 5$  respectively, for the same orifice size  $\alpha = 4.9$  and different silo size  $\xi$ . In the same figure, we also show the typical time evolution of the normalized kinetic energy of the grains  $\langle E_g^s/E_0 \rangle$  for  $\xi = 22$ . The flow starts instantaneously and, as typically observed [43],  $N(t)$  increases nearly linearly with the time for both disks and the most elongated grains assemblies. In general terms the  $N(t)$  curves nearly coincide with each other except when  $\xi$  declines toward small values. Indeed, when  $\xi$  declines while keeping  $\alpha$  constant, the parameter  $\eta$  declines too, leading to a flow equivalent to that in a pipe. For the particular case of  $(\xi, \lambda) = (10, 5)$ , we see that  $N(t)$  separates from the other curves from  $t \simeq 2000t_0$  but still showing a linear evolution with a larger slope. Figure 6(d) shows a snapshot of this case after that time, and we can see that the grains close to the walls are organized in columns and do not flow anymore, reducing “artificially” the value of the  $\eta$  parameter.

We can also observe that during the flow, the kinetic energy is a very fluctuating quantity which decreases more frequently towards 0 when the grains are most elongated. These fluctuations are largely related to reactivation of the flow during the formation of nonstable arches [see Figs. 6(a) and 6(b)]. This reactivation process is more frequent in elongated grain assemblies which are more likely to be jammed, explaining the small oscillations in the evolution of  $N(t)$ .

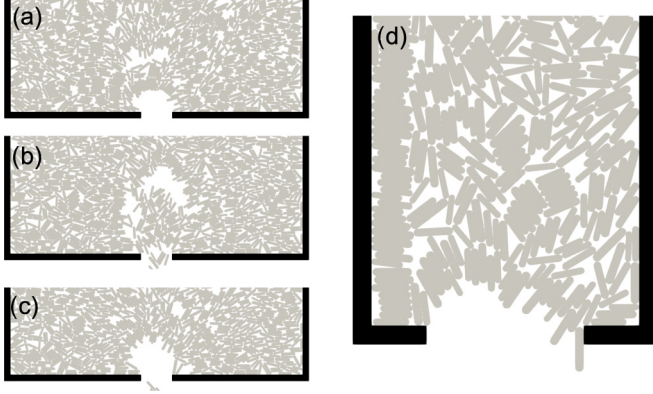


FIG. 6. Formation of dynamical (cases a and b) and static (case c) arcs for  $(\lambda, \xi) = (5, 22)$ . Illustration of RCR pile (case d) for  $(\lambda, \xi) = (5, 7)$ .

Sometimes the dynamic arches turn into static ones, causing the flow to stop [see Fig. 6(c)]. In this case, as shown on the inset in Figs. 5(a) and 5(b),  $N(t)$  is constant, the kinetic energy drops to 0, indicating that the flow is not reactivated. This results in intermittent discharge. Nevertheless, between two static arches (where the flow is reactivated following the procedure described in Sec. II), the flow can be considered stationary, for both disk and elongated grain assemblies.  $N(t)$  maintains a similar slope, which suggests that each flow period can be considered as an independent experiment. We note also that both the plateaus in kinetic energy and number of grains do not exactly start and end at the same time. This is only because the kinetic energy is computed over all grains, and thus, when a clog occurs few grains are still crossing the orifice. Thus, with a good approximation we can define the flow rate as the derivative of the linear regression on the interval where the flow is stationary:

$$Q = \frac{dN}{dt}. \quad (2)$$

In the case where static arches are formed, we eliminate the stop periods to reconstruct a new stationary discharge curve.

## B. Effects of system parameters on the flow rate

### 1. System size ( $\xi$ ; $\eta$ )

Before starting any analysis, it is important to quantify to what extent the measured flow rate  $Q$  depends on the size of the system considered. In general terms, size effects are naturally quantified according to the size of the grains; this is the  $\xi$  parameter. But in silo geometry the size effects are also intimately correlated to the  $\eta$  parameter. Indeed, let's consider two silos of different size, but with the same aperture  $D$ . The one whose  $W$  is close to  $D$  ( $\eta \rightarrow 1$ ) is more like a flow in a pipe leading to faster flow dynamics than in the  $W \gg D$  case.

Thus, in Fig. 7 we plot the evolution of  $Q$ , normalized by  $Q_{\eta \rightarrow 15}$ , the value of  $Q$  for the larger  $\eta$  at a given  $\alpha$ , as a function of  $\eta$  for the two cases  $\lambda = 1$  [Fig. 7(a)] and  $\lambda = 5$  [Fig. 7(b)] and for different normalized aperture sizes  $\alpha$ . We note that, regardless of the shape of the grains, the data collapse quite well on an exponential curve which diverges when  $\eta \rightarrow 1$  (see legend).

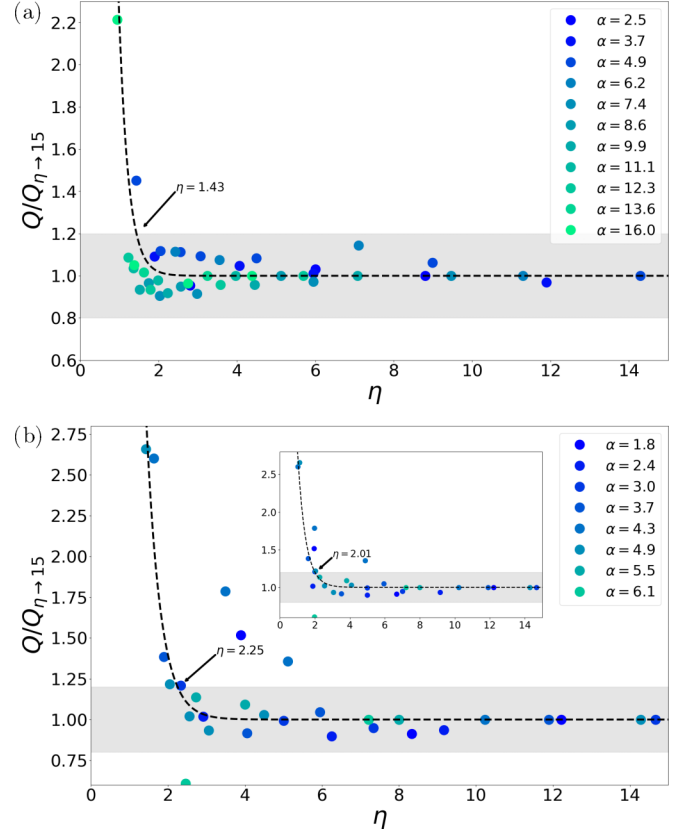


FIG. 7. Flow rate  $Q$ , normalized by  $Q_{\eta \rightarrow 15}$  the value of  $Q$  for the larger  $\eta$  at a given  $\alpha$ , as a function of  $\eta$  for  $\lambda = 1$  (a) and  $\lambda = 5$  (b) and for different values of aperture size  $\alpha$ . The inset in (b) shows the same data as (b) by correcting the value of  $\eta$  for some points according to visual inspection (see text). The dashed line is the best exponential fit of the data by  $Q \sim C_1 e^{-C_2 \eta} + 1$ , where  $C_1$  and  $C_2$  are constant values calculated with the least square method. Gray zones about the horizontal lines indicate data with less than 20% of dispersion with respect with  $Q/Q_{\eta \rightarrow 15} = 1$  that will be retained.

Nevertheless, for  $\lambda = 5$ , three points escape this rule:  $(\eta, \alpha) = \{(3.8, 1.75); (4, 1.5); (4.7, 1.37)\}$ . As illustrated by Fig. 6(d), detailed analysis of these three flows reveals a columnar structuring of the grains near the orifice. We can then estimate an equivalent  $\eta$  by arguing that these columns of grains induce a reduction of the silo thickness. The inset of Fig. 7(b) shows the evolution of  $Q$  accounting for such a correction, allowing one to shift these three points towards smaller values of  $\eta$ .

In the following, and for all the other sets of simulations that will be carried out, we make the (arbitrary) choice to keep only the data presenting a maximum dispersion of 20% around  $Q/Q_{\eta \rightarrow 15} = 1$  [gray zone in Fig. 7(a) and inset of Fig. 7(b)]. The intersection between the gray zone and the exponential fit of the data allows us to define an  $\eta_0$  above which the size effects become negligible. Simulations for values of  $\lambda$  between 1 and 7 have been conducted, and we observe that  $\eta_0$  varies approximately linearly between 1.43 and 2.01 with  $\lambda$ . Note that, for the retained data, the maximum relative error obtained by comparing linear regressions and data is at most 5%, for the point belonging to the gray zone.

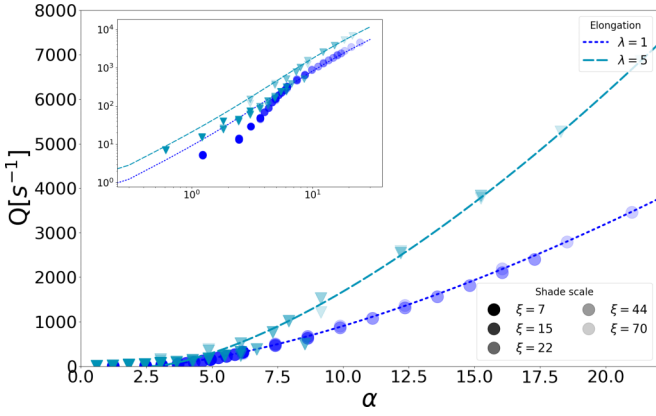


FIG. 8. Flow rate  $Q$  as a function of  $\alpha$  for  $\lambda = 1$  (blue dot) and  $\lambda = 5$  (green dot) and for  $\xi \in [7, 15, 22, 44, 70]$  (color scale). The dashed line is an approximation by the Beverloo law in the form  $Q = C\rho_g\sqrt{g}(\alpha - \kappa d)^{3/2}$ , with  $C = 408$  and  $\kappa = 1.20$  for  $\lambda = 1$  and  $C = 279$  and  $\kappa = 2.74$  for  $\lambda = 5$ . Inset: Same data but in a log scale.

Figure 8 shows, for the same set of parameters as in Fig. 7, the variation of  $Q$  as a function of  $\alpha$  for  $\xi \in [7, 15, 22, 44, 70]$  for both  $\lambda = 1$  and  $\lambda = 5$ . Note that afterwards the data where  $\eta < \eta_0(\lambda)$  have been excluded. As typically observed,  $Q$  increases with increasing orifice size  $\alpha$ . Our data are well approximated by Beverloo’s law including for very elongated grains (dashed lines; see legend). Most importantly, we find that  $Q$  is independent of the silo size  $\xi$  even for the most elongated grains, and at least for the silo sizes simulated in this work. We also note that the flow rate is higher for elongated grains than for disks. This last observation is discussed with more detail in the next section in the light of the normalization used for  $\alpha$ .

## 2. Grain shape and orifice size

Once we show that  $Q$  is independent of the silo size, we can fix  $\xi$  to study the effect of grains’ elongation on the flow rates. We choose an intermediate value to combine the possibility of a large aperture range satisfying  $\eta > \eta_0(\lambda)$  and shorter time of simulation. We take  $\xi = 44$ , while increasing both the grain aspect ratio  $\lambda$  and the normalized orifice size  $\alpha$ . As shown in Fig. 8, we find that for all shapes  $Q$  is an increasing function of  $\alpha$ . After having shown that our data are well approximated by Beverloo’s equation (see Fig. 8), we evidence here that, for all shapes, our data are also well fitted by the Janda model [Eq. (12); dashed lines in Fig. 9], whose development will be discussed in more detail in Sec. IV in correlation with the velocity and packing fraction profiles. Also, and as a general observation, we find that the flow rate is higher with increasing  $\lambda$ . It is consistent with some previous work [29] but contrasts with others [30]. In fact, the increasing or decreasing behavior of  $Q$  with grain elongation is mainly due to the way the orifice size is normalized. To support this statement, in the inset of Fig. 9 we display the same data as a function of  $\bar{\alpha} = D/\langle d \rangle$  corresponding to the orifice size normalized by the mean diameter of disks. In this case, consistently with [44],  $Q$  is a decreasing function of  $\lambda$ . Having identified the origin of the discrepancy observed in the literature, in the following we continue with the  $\alpha$  parameter.

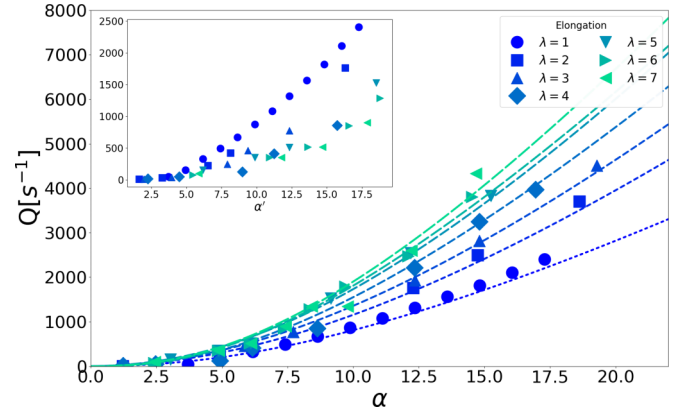


FIG. 9. Flow rate  $Q$  as a function of  $\alpha$  for  $\xi = 44$  and increasing  $\lambda \in [1, 2, 3, 4, 5, 6, 7]$ . The dashed lines are approximations given by Eq. (12) (see Sec. IV C). The inset shows the same data all plotted as a function of  $\bar{\alpha} = D/\langle d \rangle$ , i.e., the orifice size normalized by the mean disk diameter  $\langle d \rangle$  instead of normalizing by  $L$  for  $\lambda > 1$ .

Figure 10 displays the variation of  $Q$  as a function of  $\lambda$  for increasing values of  $\alpha$ . For small orifice size (i.e., for  $\alpha$  below  $\sim 6.5$ ),  $Q$  is relatively independent of  $\lambda$ . For intermediate values of  $\alpha$ , typically  $\alpha \in [\sim 7, \sim 12]$ ,  $Q$  first increases with  $\lambda$  but saturates toward an  $\alpha$ -dependent value as grains become more elongated. Finally, for larger values of  $\alpha > 12$ ,  $Q$  is an increasing function of  $\lambda$ . Note that for identical  $\bar{\alpha}$  an opposite behavior is obtained. This behavior is quite surprising as it suggests that a “small” departure from circular shape has stronger effects on  $Q$  than larger shape deviations.

This point is discussed in more detail below, when we analyze the velocity and packing fraction profiles close to the orifice.

## IV. FLOW PATTERNS

In this section we focus on the effects of system parameters on velocity and packing fraction profiles close to the orifice. The corresponding profiles are obtained according to a similar methodology presented in [17]. Basically, for the velocity profiles a fictitious zone of length  $D$  and thickness  $\bar{d}$  is considered

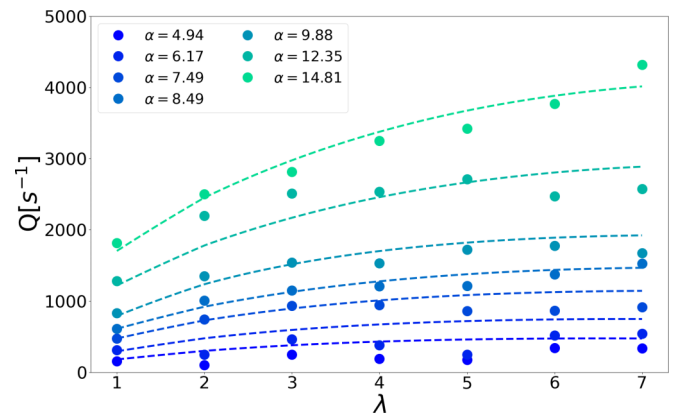


FIG. 10. Flow rate  $Q$  as a function of  $\lambda$  for various  $\alpha = D/\langle d \rangle$ . Dashed lines are the approximations given by Eq. (13) (see Sec. IV C).



FIG. 11. Area of calculation for velocity profile (a) and packing fraction profile (b).

around the orifice and divided into  $n_c$  columns; see Fig. 11(a). When a grain crosses this zone (identified by its center of mass), both its velocity and its position are recorded. For the packing fraction, and in order to have a better statistical description, a square fictitious zone of length  $D$ , divided into  $n_c$  columns, is used; see Fig. 11(b). The packing fraction for each subcolumn is obtained by computing the exact surface of the grains crossing the corresponding subcolumn. For both the velocity and packing fraction profiles,  $n_c$  is fixed to  $\frac{D}{0.1\langle d \rangle}$ . The final velocity and packing fraction profiles are achieved by time averaging the profiles over all recorded data.

**A. Velocity profiles**

The vertical velocity profiles,  $v_y(x)$ , for different normalized orifice sizes  $\alpha$  and for increasing system sizes  $\xi$  are presented in Fig. 12 for  $\lambda = 1$  (column left) and  $\lambda = 5$  (column right). Regardless of the value of  $\xi$ , the velocity profiles show a parabolic-like profile as observed for assemblies of disks [17] or slightly elongated grains [44]. The velocity at the center of the orifice (i.e., for  $x = 0$ ),  $v_c$ , increases as the normalized orifice size increases. The self-similar behavior of the velocity profiles is verified by normalizing  $v_y$  by  $v_c$  and  $x$  by  $R = 0.5\alpha\bar{d}$ . We find that for both disks and for

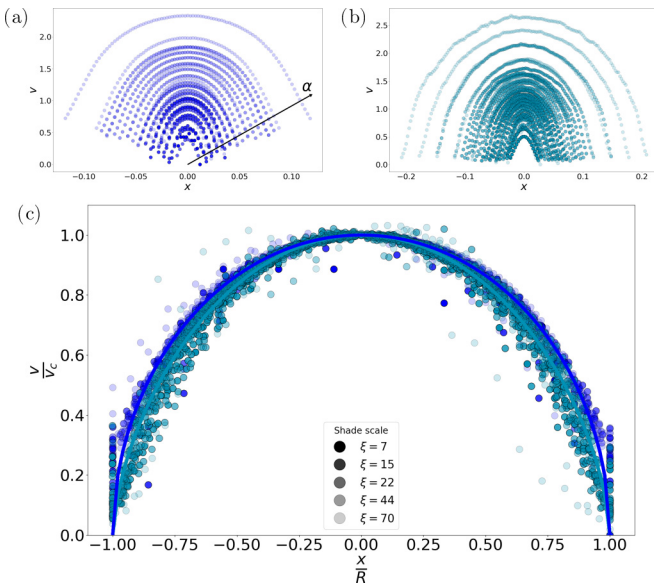


FIG. 12. Velocity profiles (first row) and normalized velocity profiles (second row)  $v_y(x)/v_c$  measured close to the orifice for  $\lambda = 1$  (left column) and  $\lambda = 5$  (right column) with increasing orifices size  $\alpha$ . The second row illustrates the self-similarity of the profiles as a function of system size for all  $\alpha$ . Continuous lines are the approximations given by Eq. (3).

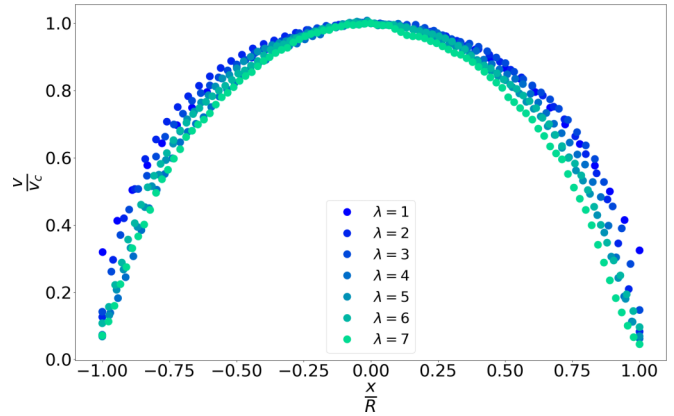


FIG. 13. Normalized velocity profiles for  $\xi = 44$ ,  $\alpha = 6.17$  and increasing  $\lambda$ .

$\lambda = 5$ , all data collapse on a master curve, proving that the main features of the velocity profiles are not influenced by the size of the system or by the size of the orifice. Concerning the effects of grain shape, we find that the velocity profiles become narrower around the center of the orifice as grain elongation increases; see Fig. 13. The velocity at the edges of the orifice decreases with grain elongation, mainly due to the columnar arrangement of the grains near the bottom (as shown in Fig. 6), thereby reducing flow velocities.

In agreement with previous work [45], the normalized velocity profiles are fitted by the following equation:

$$v(x) = v_c(\alpha, \lambda) \left[ 1 - \left( \frac{x}{R} \right)^2 \right]^{-\mu_\lambda}, \quad (3)$$

where  $R = 0.5\alpha\bar{d}$ ,  $\mu_\lambda$  is a fitting parameter that depends only on  $\lambda$  (see Table II), and  $v_c$  depends on  $\alpha$  and  $\lambda$ .

Figure 14 shows the evolution of  $v_c$  as a function of  $\alpha$  for different values of  $\lambda$ . In general terms, for all shapes,  $v_c$  is an increasing function of  $\alpha$ . Assuming a free-fall of the grains of a typical height of the order of the effective cross section, we see that  $v_c \propto \gamma\sqrt{2gR} = \gamma\sqrt{g\alpha\bar{d}}$ , with  $\gamma$  a fitting parameter. Although this prediction is well verified for quasimonodisperse disk flows [17], it seems to be less accurate in size-disperse systems [20] or when grain shape deviates, even slightly, from circular shape [44]. This is also the case in our simulations as shown in the inset of Fig. 14 for  $\lambda = 1$  and  $\lambda = 4$ , in which a slight, but nonzero, deviation of the prediction with respect to our data is observed. A plausible explanation, as suggested by the snapshots in Fig. 6 and investigated in more detail by Börzsönyi *et al.* [46], is that arches' heights depend on both grain shapes and grain sizes, challenging the hypothesis of a constant typical height during the ballistic fall. Following the work of Zhou *et al.* [20], we can propose, for a fixed value of  $\lambda$ , a better approximation of

TABLE II. Fitting parameters entering in Eq. (3) and in Eq. (4).

$\lambda$	1	2	3	4	5	6	7
$\mu_\lambda$	1.98	2.19	1.99	1.67	1.59	1.40	1.38
$\gamma_\lambda$	1.50	1.40	1.34	1.33	1.33	1.32	1.31



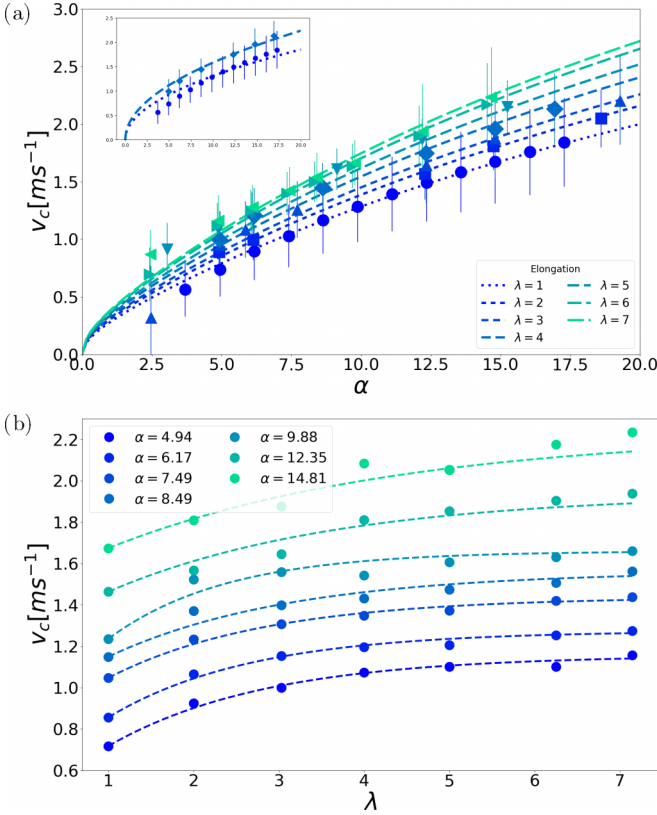


FIG. 14. Velocity  $v_c$  measured at the center of the orifice as a function of  $\alpha$  for all  $\lambda$  (a) and as a function of  $\lambda$  for various orifice size  $\alpha$  (b) both for  $\xi = 44$ . The values of  $v_c$  for various  $\xi$  are also shown in color scale only for  $\lambda = 1$  and  $\lambda = 5$ . The dashed lines are the approximations given by Eq. (4) (a) and Eq. (5) (b). The inset in (a) shows the same data as the main plot approximated by the free-fall arches model  $\gamma\sqrt{g\alpha d}$ , with  $\gamma$  the “best” fitting parameter minimizing the error between the data and the prediction.

$v_c$  as a function of  $\alpha$ :

$$v_c(\alpha) = \gamma_\lambda \sqrt{g\alpha d} (1 - \beta_1 e^{-\beta_2 \alpha}), \quad (4)$$

with  $\gamma_\lambda$ ,  $\beta_1$ , and  $\beta_2$  as fitting parameters, where  $\gamma_\lambda$  declines from 1.52 to 1.32 as  $\lambda$  increases (see Table II), while  $\beta_1$  and  $\beta_2$  are found to be independent of  $\lambda$  and equal to 0.45 and 0.13, respectively. These values are not so far from the ones obtained by Gao *et al.* [44] with weakly elongated ellipses.

The effect of grain shape on arch height is also well captured when we plot  $v_c$  as a function of  $\lambda$  for different  $\alpha$ ; see Fig. 14(b). Interestingly,  $v_c$  evolves in a nonlinear way with  $\lambda$ :  $v_c$  first increases with  $\lambda$  from  $v_c^{\alpha,1}$  (i.e., the velocity at the orifice center measured in disk flows case at different  $\alpha$ ), and then saturates towards an  $\alpha$ -dependent value  $v_c^{\alpha,\infty}$ ; see also Table II. For all  $\alpha$ , our numerical data are well fitted by the exponential function

$$v_c(\lambda) = v_c^{\alpha,1} + (v_c^{\alpha,\infty} - v_c^{\alpha,1}) [1 - e^{-(\lambda-1)/\lambda_c^\alpha}], \quad (5)$$

with  $\lambda_c^\alpha$  a fitting parameter that varies between 1.88 and 3.42 as  $\alpha$  increases.

The increase of  $v_c$  with  $\lambda$  and its saturation indicates that, on average, the height of the arches increases when the shapes slightly deviate from circular ones, but a critical size of the

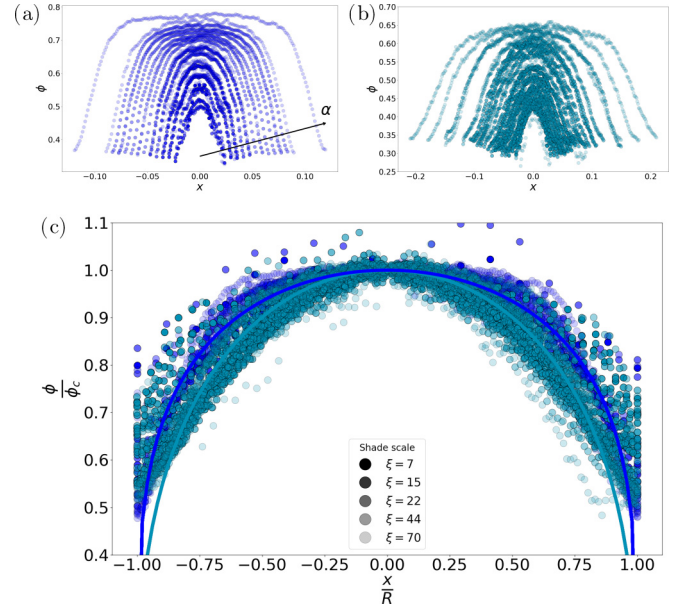


FIG. 15. Packing fraction profiles  $\phi(x)$  measured close to the orifice for  $\lambda = 1$  (a) and  $\lambda = 5$  (b) with increasing orifice size  $\alpha$  and system size  $\xi$  (color level). Normalized packing fraction profiles  $\phi(x)/\phi_c$  all  $\alpha$  and  $\xi$  (c).

arches cannot be exceeded even by strongly increasing the aspect ratio of the grains.

## B. Packing fraction profiles

Along with the velocity profiles, the profiles of a packing fraction close to the orifice,  $\phi(x)$ , for various normalized orifice sizes  $\alpha$  and for increasing system sizes  $\xi$  are shown in Fig. 15 for  $\lambda = 1$  (a) and  $\lambda = 5$  (b). As typically observed, the packing fraction profiles adopt a “bell” shape with a sharp peak  $\phi_c$  around  $x = 0$ , which progressively widens as  $\alpha$  increases, both in disk flows and in very elongated grain flows.

Also, we find that the packing fraction increases with increasing  $\alpha$ , whether for  $\lambda = 1$  or  $\lambda = 5$ . The self-similar behavior of the packing fraction profiles is also verified by normalizing  $\phi(x)$  by  $\phi_c$  and  $x$  by  $R$ ; see Fig. 12(c). As for the velocity profiles, for a given grain shape we find that all data collapse on a master curve, which evidences that the main features of the packing fraction profiles are not influenced by the system size and orifice size. Yet grain elongation induces a slight narrowing of the packing fraction profiles around  $x = 0$ , as better illustrated in Fig. 16.

The normalized packing fraction profiles are fitted by the following equation [17]:

$$\phi(x) = \phi_c(\alpha, \lambda) \left[ 1 - \left( \frac{x}{R} \right)^2 \right]^{-\nu_\lambda}, \quad (6)$$

where  $\nu_\lambda$  is a fitting parameter that depends on  $\lambda$  (see Table III), and  $\phi_c$  that depends *a priori* on  $\alpha$  and  $\lambda$ .

Figure 17 shows the evolution of  $\phi_c$  as a function of both  $\alpha$  and  $\lambda$ . We see that, for all shapes,  $\phi_c$  evolves asymptotically with  $\alpha$  towards an  $\lambda$ -dependent value  $\phi_c^{\lambda,\infty}$  that declines from 0.78 to 0.68 as  $\lambda$  increases from 1 to 7 (see details in Table III). This result extends to the case of elongated grains a result

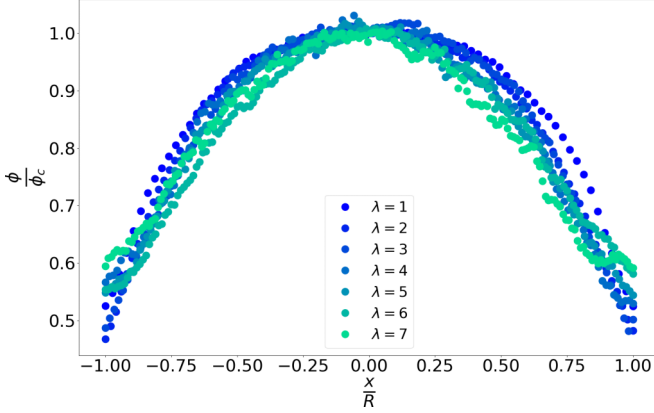


FIG. 16. Normalized packing fraction profiles for  $\xi = 44$  and increasing  $\lambda$  at  $\alpha = 6.17$ . Continuous lines are the approximations given by Eq. (6).

previously obtained for disks [17] or for weakly elongated ellipses [44,47]. Consistent with previous works, our numerical data are well approximated by the following expression [17]:

$$\phi_c(\alpha) = \phi_c^{\lambda, \infty} (1 - A_\lambda e^{-\frac{\alpha \bar{d}}{B_\lambda}}), \quad (7)$$

where  $A_\lambda$  and  $B_\lambda$  are fitting parameters summarized in Table III.

In contrast,  $\phi_c$  seems to be independent of  $\lambda$  while  $\lambda \leq 2$ , and beyond that,  $\phi_c$  decreases linearly with  $\lambda$ ; and our numerical data are well approximated by

$$\phi_c(\lambda) = \phi_c^{\alpha, 1} + \beta_3(\lambda - 2)\delta_{\lambda > 2}, \quad (8)$$

where  $\delta_{\lambda > 2}$  is a ‘‘Kronecker-like’’ parameter equal to 0 if  $\lambda \in [1, 2]$  or equal to 1 otherwise,  $\phi_c^{\alpha, 1}$  is the packing fraction for  $\lambda = 1$  at a fixed value of  $\alpha$  [see Fig. 17(a)], and  $\beta_3$  is a fitting parameter found to be independent with grains elongation, system size, or normalized orifice size and equal to  $\sim -0.033$ . It should be noted that the choice to consider  $\phi_c$  constant for  $\lambda \in [1, 2]$  is also motivated by several previous works in which it is shown that the packing fraction varies nonlinearly with grain elongation [22,48–50]: it first increases slightly with grain elongation while  $\lambda \leq 2$ , but declines as the grains become more elongated, as also observed in our simulations. Equation (8) could then be refined over the interval  $\lambda \in [1, 2]$ , but this is beyond the scope of this work, and we consider it as constant.

### C. Revisiting the Janda equation

The velocity and packing fraction profiles described above are interesting not only as quantitative descriptors of local

TABLE III. Fitting parameters entering in Eq. (6) and in Eq. (7).

$\lambda$	1	2	3	4	5	6	7
$v_\lambda$	4.25	4.43	4.36	3.75	2.75	2.61	3.29
$A_\lambda$	0.65	0.70	0.75	0.82	0.77	0.91	0.97
$B_\lambda$	0.055	0.074	0.081	0.092	0.103	0.102	0.115
$\phi_c^{\lambda, \infty}$	0.77	0.76	0.71	0.68	0.67	0.62	0.61

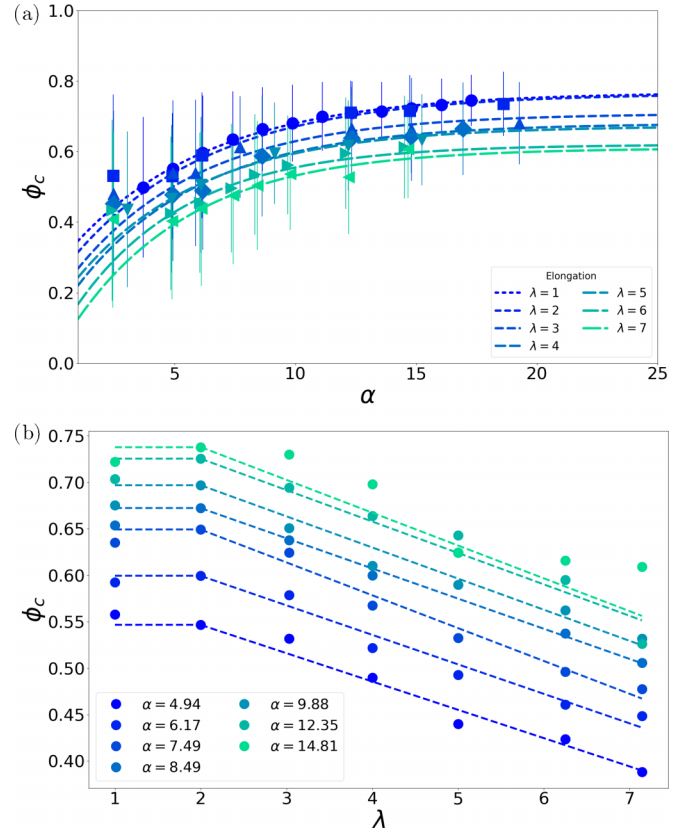


FIG. 17. Packing fraction  $\phi_c$  measured at the center of the orifice as a function of  $\alpha$  for all  $\lambda$  (a) and as function of  $\lambda$  for various orifice sizes  $\alpha$  (b). The dashed lines are the approximations given by Eq. (7) (a) and by Eq. (8) (b).

features of the flows, but more fundamentally because, as shown by Janda *et al.* [17], when combined they allow one to explain the evolution of the flow rate with  $\alpha$  and, as we will see, with  $\lambda$  too.

Indeed, let’s remark that the flow rate  $Q$ , in its regular form, is given by

$$Q = 2 \int_0^{D/2} \frac{1}{\mathcal{A}} \phi(x) v(x) dx, \quad (9)$$

where  $\mathcal{A}$  is the mean grain surface, which is fixed constant and equal to  $\mathcal{A}_d$  in this study. Then, by injecting Eq. (3) and Eq. (6) into Eq. (9), we get

$$Q(\alpha, \lambda) = \frac{2}{\mathcal{A}} v_c(\alpha, \lambda) \phi_c(\alpha, \lambda) \int_0^{D/2} \left(1 - \left(\frac{x}{R}\right)^2\right)^{\frac{v_\lambda + \mu_\lambda}{v_\lambda \mu_\lambda}} dx, \quad (10)$$

Then, remarking that the integral in Eq. (10) can be rewritten in terms of the  $\beta$  function as  $\alpha \bar{d} \beta(1/2; (v_\lambda + \mu_\lambda)/v_\lambda \mu_\lambda + 1)$ , and recalling that  $R = 0.5 \bar{d} \alpha$ , we obtain the following general expression for the flow rate:

$$Q(\alpha, \lambda) = \Psi(\lambda) v_c(\alpha, \lambda) \phi_c(\alpha, \lambda) \alpha, \quad (11)$$

with  $\Psi(\lambda) = \frac{1}{\mathcal{A}} \beta\left(\frac{1}{2}; \frac{v_\lambda + \mu_\lambda}{v_\lambda \mu_\lambda} + 1\right) \bar{d}$ , which remains constant with respect with  $\alpha$ . Note that, as shown in Fig. 18, the  $\beta$  function slightly evolves with  $\lambda$ , and thus, for the sake of simplicity, we will set it equal to its mean value,  $\beta^* \sim 1.4$ . Moreover,

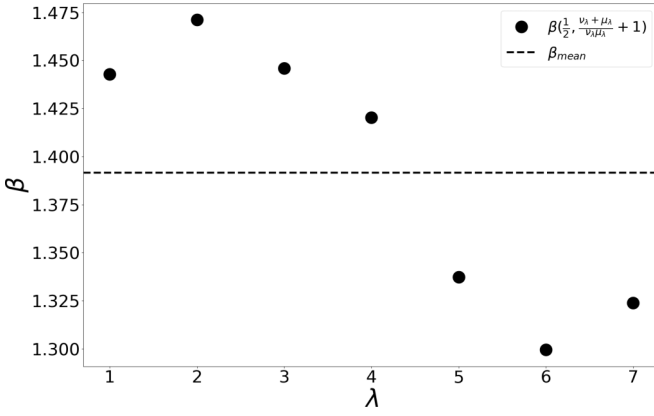


FIG. 18. Evolution of the  $\beta$  function  $\beta(\frac{1}{2}; \frac{v_\lambda + \mu_\lambda}{v_\lambda \mu_\lambda} + 1)$  as a function of  $\lambda$ . The dashed line is the mean values  $\beta^*$  of the data.

it should be noted that, following the choice made to build the particles, we get  $\bar{d}/\mathcal{A} = 2\lambda/[d\sqrt{\pi}(\pi + 2\lambda - 2)]$ . Thus, in the following we set  $\Psi(\lambda) \simeq 2\lambda\beta^*/[d\sqrt{\pi}(\pi + 2\lambda - 2)]$ .

Thus, it becomes easy to obtain a theoretical expression for the flow rate  $Q$  as a function of  $\alpha$  and for a fixed  $\lambda$  value, by introducing Eqs. (4) and (7) into Eq. (11):

$$Q_\lambda(\alpha) = \Psi'_\lambda [1 - \beta_1 e^{-\beta_2 \frac{\alpha}{2}}] [1 - A_\lambda e^{-\frac{\alpha \bar{d}}{b_\lambda}}] \alpha^{3/2}, \quad (12)$$

with  $\Psi'_\lambda = \Psi(\lambda)\phi_c^{\lambda, \infty} \gamma_\lambda \sqrt{gd}$ . The prediction given by Eq. (12) is shown in Fig. 9. As expected, we see a fair approximation of the evolution of the flow rate as function of  $\alpha$  for all values of  $\lambda$ . Equation (12) extends to the case of highly elongated grains a previous model established by Janda *et al.* [17] for circular grains.

In the same way, a theoretical expression for the flow rate  $Q$  as a function of  $\lambda$ , and at a fixed value of  $\alpha$ , can be obtained by introducing Eqs. (5) and (8) into Eq. (11):

$$Q_\alpha(\lambda) = \Psi(\lambda) [v_c^{\alpha, 1} + (v_c^{\alpha, \infty} - v_c^{\alpha, 1})(1 - e^{-(\lambda-1)/\lambda^\alpha})] \times [\phi_c^{\alpha, 1} + \beta_3(\lambda - 2)\delta_{\lambda > 2}] \frac{\alpha}{2}, \quad (13)$$

where  $\Psi(\lambda)$  increases from  $\sim 1/d$  to  $\sim 2/d$  as  $\lambda$  is increased.

As shown in Fig. 10, Eq. (13) provides a fairly good approximation of our data for all values of  $\alpha$ . Equation (13) allows us to better understand the nonlinear variation of  $Q$  as a function of  $\lambda$ . At small normalized orifice sizes, the decreases in  $\phi_c$  compensate for the increases in  $v_c$  and to a lesser extent the increases in  $\Psi$ , explaining the near independence of  $Q$  with  $\lambda$ . At larger orifice sizes, the rapid increase in  $Q$  is mainly due to the increase in  $v_c$  and  $\Psi$ , while its saturation at larger  $\lambda$  values results from the decrease in  $\phi_c$ , which compensates for the increase in  $v_c$  and, to a lesser extent, the increase of  $\Psi$ .

## V. CONCLUSIONS

In this paper, using 2D contact dynamics simulations, we investigated the combined effects of grain shape and system size on the grain flow in silo for increasing orifice sizes. The grain shapes are rounded-cap rectangles characterized by their aspect ratio  $\lambda$  that varies continuously from a 1

(disk) to 7 (thin rectangle with rounded caps). The size of the silo is characterized by its width, which is varied from 7 to 70 times the size of the grains. In order to isolate the effects of grain shape and system size, both the mass and surface of the grains are kept constant as well as the total mass of the system and the condition of the discharge.

By simulating a large number of avalanches, the flow rates, velocity profiles, and packing fraction profiles are systematically studied as a function of characteristic dimensionless numbers, such the aspect ratio of the grains, the orifice size normalized by the grain size, and the system size normalized either by the orifice size or by the grain size.

A central finding of this work is that the flow rate of elongated grain assemblies increases as a Beverloo-like or a Janda-like function as the orifice size is increased. In contrast, the effect of grain elongation on the flow rate depends on the normalized orifice size. For small orifice sizes, the flow rate is independent with grain elongation. In contrast, at larger orifice sizes, the flow rate first increases with grain elongation, but it may saturate or continue to increase at larger grain aspect ratio.

In general, neither the shape of the grains nor the size of the systems affects the general form of the packing fraction and velocity profiles. They all present a self-similar behavior when normalized by a critical packing fraction or a critical velocity, respectively, measured at the center of the orifice. On the other hand, these critical velocities and packing fraction depend strongly on the shape of the grains. In particular, the packing fraction at the center decreases with grain elongation, while the velocity at the center increases and saturates at large grain elongations. It is precisely the competition between these two behaviors that explains the nonlinear variation of the flow rate as a function of the grain shape and for a given orifice size.

These results can be extended in different directions. These results need to be validated experimentally. In this case, it would be possible to reproduce the 2D experimental approach developed by Janda *et al.* considering grains of different elongations. The 2D numerical work presented here would make it possible to calibrate the experiment sizes for each shape in order to avoid scale effects. A question that still remains open is the extension of the approach proposed by Janda to 3D geometries. In this case, 3D profiles must be reconstructed. One can imagine that the self-similarity behavior of these profiles will continue to be verified with spheres [51]. For elongated grains, the flow is generally more complex [52]. In silo geometry it is reported that the flow of elongated grains is increasingly intermittent as the aspect ratio of the grains is increased [53] given the greater possibilities offered to the grains to orient themselves in space. As a result, packing fraction and velocity profiles could be also increasingly correlated in time with each other not only in the bulk, but also close to the orifice, making the integration of Eq. (8) more complex, as time effects would have to be taken into account. 3D simulations are currently underway with rodlike grains to address this issue, and results will be presented in a forthcoming publication.

We have also seen that elongated grains tend to form rigid columns especially near the walls. It would then be useful to

revisit these results for silos with an inclined bottom. Finally, in this paper we have not addressed the issues of clogging statistics (including their number and arch shape) as a function of grain shape. This analysis is in progress and will be presented in a future publication.

## ACKNOWLEDGMENTS

The authors acknowledge financial support by ANRT (Convention Cifre 2021-0256). We also acknowledge the support of the High-Performance Computing Platform MESO@LR.

- 
- [1] T. Pongó, V. Stiga, J. Török, S. Lévy, B. Szabó, R. Stannarius, R. C. Hidalgo, and T. Börzsönyi, Flow in an hourglass: particle friction and stiffness matter, *New J. Phys.* **23**, 023001 (2021).
- [2] T. Xu, J. Yu, Y. Yu, and Y. Wang, A modelling and verification approach for soybean seed particles using the discrete element method, *Adv. Powder Technol.* **29**, 3274 (2018).
- [3] C. Campbell, Granular material flows—An overview, *Powder Technol.* **162**, 208 (2006).
- [4] G. Gutiérrez, C. Colonnello, P. Boltenhagen, J. Darias, R. Peralta-Fabi, F. Brau, and E. Clément, Silo collapse under granular discharge, *Phys. Rev. Lett.* **114**, 018001 (2015).
- [5] H. Janssen, Versuche über Getreidedruck in Silozellen (1895), p. 1045.
- [6] C. Perge, M. A. Aguirre, P. A. Gago, L. A. Pugnali, D. Le Tourneau, and J.-C. Géminard, Evolution of pressure profiles during the discharge of a silo, *Phys. Rev. E* **85**, 021303 (2012).
- [7] A. Hafez, Q. Liu, T. Finkbeiner, R. A. Alouhali, T. E. Moellendick, and J. C. Santamarina, The effect of particle shape on discharge and clogging, *Sci. Rep.* **11**, 3309 (2021).
- [8] W. A. Beverloo, H. A. Leniger, and J. van de Velde, The flow of granular solids through orifices, *Chem. Eng. Sci.* **15**, 260 (1961).
- [9] J. R. Valdes and J. C. Santamarina, Clogging: Bridge formation and vibration-based destabilization, *Can. Geotech. J.* **45**, 177 (2008).
- [10] E. Goldberg, C. Manuel Carlevaro, and L. A. Pugnali, Clogging in two-dimensions: Effect of particle shape, *J. Stat. Mech.* (2018) 113201.
- [11] I. Zuriguel, A. Janda, A. Garcimartín, C. Lozano, R. Arévalo, and D. Maza, Silo clogging reduction by the presence of an obstacle, *Phys. Rev. Lett.* **107**, 278001 (2011).
- [12] K. Endo, K. A. Reddy, and H. Katsuragi, Obstacle-shape effect in a two-dimensional granular silo flow field, *Phys. Rev. Fluids* **2**, 094302 (2017).
- [13] C. Mankoc, A. Garcimartín, I. Zuriguel, D. Maza, and L. A. Pugnali, Role of vibrations in the jamming and unjamming of grains discharging from a silo, *Phys. Rev. E* **80**, 011309 (2009).
- [14] T. Pongó, T. Börzsönyi, and R. Cruz Hidalgo, Discharge of elongated grains in silos under rotational shear, *Phys. Rev. E* **106**, 034904 (2022).
- [15] R. Kobylka, J. Wikacek, P. Parafiniuk, J. Horabik, M. Banda, M. Stasiak, and M. Molenda, Discharge flow of spherical particles from a cylindrical bin: Experiment and simulations, *Processes* **9**, 1860 (2021).
- [16] A. Garcimartín, C. Mankoc, A. Janda, R. Arévalo, J. M. Pastor, I. Zuriguel, and D. Maza, Flow and jamming of granular matter through an orifice, in *Traffic and Granular Flow '07*, edited by C. Appert-Rolland, F. Chevoir, P. Gondret, S. Lassarre, J.-P. Lebacque, and M. Schreckenberg (Springer, Berlin, 2009), pp. 471–486.
- [17] A. Janda, I. Zuriguel, and D. Maza, Flow rate of particles through apertures obtained from self-similar density and velocity profiles, *Phys. Rev. Lett.* **108**, 248001 (2012).
- [18] C. Mankoc, A. Janda, R. Arévalo, J. M. Pastor, I. Zuriguel, A. Garcimartín, and D. Maza, The flow rate of granular materials through an orifice, *Granular Matter* **9**, 407 (2007).
- [19] M. Benyamine, M. Djermane, B. Dalloz-Dubrujeaud, and P. Aussillous, Discharge flow of a bidisperse granular media from a silo, *Phys. Rev. E* **90**, 032201 (2014).
- [20] Y. Zhou, P. Ruyer, and P. Aussillous, Discharge flow of a bidisperse granular media from a silo: Discrete particle simulations, *Phys. Rev. E* **92**, 062204 (2015).
- [21] G. Lu, J. Third, and C. Müller, Discrete element models for non-spherical particle systems: From theoretical developments to applications, *Chem. Eng. Sci.* **127**, 425 (2015).
- [22] E. Azéma and F. Radjaï, Stress-strain behavior and geometrical properties of packings of elongated particles, *Phys. Rev. E* **81**, 051304 (2010).
- [23] E. Azéma, N. Estrada, and F. Radjaï, Nonlinear effects of particle shape angularity in sheared granular media, *Phys. Rev. E* **86**, 041301 (2012).
- [24] T. Binaree, E. Azéma, N. Estrada, M. Renouf, and I. Preechawuttipong, Combined effects of contact friction and particle shape on strength properties and microstructure of sheared granular media, *Phys. Rev. E* **102**, 022901 (2020).
- [25] R. C. Hidalgo, I. Zuriguel, D. Maza, and I. Pagonabarraga, Role of particle shape on the stress propagation in granular packings, *Phys. Rev. Lett.* **103**, 118001 (2009).
- [26] T. Kanzaki, M. Acevedo, I. Zuriguel, I. Pagonabarraga, D. Maza, and R. C. Hidalgo, Stress distribution of faceted particles in a silo after its partial discharge, *Eur. Phys. J. E* **34**, 133 (2011).
- [27] E. Azéma and F. Radjaï, Force chains and contact network topology in sheared packings of elongated particles, *Phys. Rev. E* **85**, 031303 (2012).
- [28] J. Tang and R. P. Behringer, Orientation, flow, and clogging in a two-dimensional hopper: Ellipses vs. disks, *Europhys. Lett.* **114**, 34002 (2016).
- [29] P. A. Langston, M. A. Al-Awamleh, F. Y. Fraige, and B. N. Asmar, Distinct element modelling of non-spherical frictionless particle flow, *Chem. Eng. Sci.* **59**, 425 (2004).
- [30] S. Liu, Z. Zhou, R. Zou, D. Pinson, and A. Yu, Flow characteristics and discharge rate of ellipsoidal particles in a flat bottom hopper, *Powder Technol.* **253**, 70 (2014).
- [31] P. W. Cleary and M. L. Sawley, DEM modelling of industrial granular flows: 3D case studies and the effect of particle shape on hopper discharge, *Appl. Math. Modell.* **26**, 89 (2002).
- [32] P. W. Cleary, The effect of particle shape on hopper discharge, in *Second International Conference on CFD in the Minerals and Process Industries* (CSIRO, Australia, 1999), pp. 71–76.
- [33] T. Pongó, B. Fan, D. Hernández-Delfin, J. Török, R. Stannarius, R. C. Hidalgo, and T. Börzsönyi, The role of the particle aspect

- ratio in the discharge of a narrow silo, *New J. Phys.* **24**, 103036 (2022).
- [34] J. J. Moreau, Unilateral contact and dry friction in finite freedom dynamics, in *Nonsmooth Mechanics and Applications* (Springer, Berlin, 1988), pp. 1–82.
- [35] M. Jean, The non-smooth contact dynamics method, *Comput. Methods Appl. Mech. Eng.* **177**, 235 (1999).
- [36] M. Renouf, F. Dubois, and P. Alart, A parallel version of the non smooth contact dynamics algorithm applied to the simulation of granular media, *J. Comput. Appl. Math.* **168**, 375 (2004).
- [37] F. Dubois, V. Acary, and M. Jean, The contact dynamics method: A nonsmooth story, *C.R. Mec.* **346**, 247 (2018).
- [38] F. Dubois and M. Jean, The non smooth contact dynamic method: Recent LMG90 software developments and application, in *Analysis and Simulation of Contact Problems*, edited by P. Wriggers and U. Nackenhorst, Lecture Notes in Applied and Computational Mechanics Vol. 27 (Springer, Berlin, 2006), pp. 375–378.
- [39] P. Sanchez, M. Renouf, E. Azéma, R. Mozul, and F. Dubois, A contact dynamics code implementation for the simulation of asteroid evolution and regolith in the asteroid environment, *Icarus* **363**, 114441 (2021).
- [40] R. M. Nedderman, U. Tuzen, S. B. Savage, and G. T. Houlsby, Flow of granular materials—I: Discharge rates from hoppers, *Chem. Eng. Sci.* **37**, 1597 (1982).
- [41] R. L. Brown, Profile of flow of granules through apertures, *Trans. Instn. Chem. Engrs.* **38**, 243 (1960).
- [42] R. Arévalo and I. Zuriguel, Clogging of granular materials in silos: Effect of gravity and outlet size, *Soft Matter* **12**, 123 (2016).
- [43] Y. Xu, K. D. Kafui, C. Thornton, and G. Lian, Effects of material properties on granular flow in a silo using DEM simulation, *Part. Sci. Technol.* **20**, 109 (2002).
- [44] Q. Gao, Y. Chen, and C. Zhao, Self-similarity of density and velocity profiles in a 2D hopper flow of elliptical particles: Discrete element simulation, *Powder Technol.* **402**, 117338 (2022).
- [45] D. Gella, D. Maza, and I. Zuriguel, Role of particle size in the kinematic properties of silo flow, *Phys. Rev. E* **95**, 052904 (2017).
- [46] T. Börzsönyi, E. Somfai, B. Szabó, S. Wegner, P. Mier, G. Rose, and R. Stannarius, Packing, alignment and flow of shape-anisotropic grains in a 3D silo experiment, *New J. Phys.* **18**, 093017 (2016).
- [47] C. Li, X. Li, T. Jiao, F. Hu, M. Sun, and D. Huang, Influence of grain bidispersity on dense granular flow in a two-dimensional hopper, *Powder Technol.* **401**, 117271 (2022).
- [48] W. Man, A. Donev, F. H. Stillinger, M. T. Sullivan, W. B. Russel, D. Heeger, S. Inati, S. Torquato, and P. M. Chaikin, Experiments on random packings of ellipsoids, *Phys. Rev. Lett.* **94**, 198001 (2005).
- [49] A. Donev, R. Connelly, F. H. Stillinger, and S. Torquato, Underconstrained jammed packings of nonspherical hard particles: Ellipses and ellipsoids, *Phys. Rev. E* **75**, 051304 (2007).
- [50] A. V. Kyrylyuk, M. Anne van de Haar, L. Rossi, A. Wouterse, and A. P. Philipse, Isochoric ideality in jammed random packings of non-spherical granular matter, *Soft Matter* **7**, 1671 (2011).
- [51] D. Maza, A. Janda, S. M. Rubio-Largo, I. Zuriguel, and R. C. Hidalgo, Velocity and density scaling at the outlet of a silo and its role in the expression of the mass flow rate, *AIP Conference Proceedings* (American Institute of Physics, Sydney, Australia, 2013), Vol. 1542, pp. 674–677.
- [52] D. B. Nagy, P. Claudin, T. Börzsönyi, and E. Somfai, Rheology of dense granular flows for elongated particles, *Phys. Rev. E* **96**, 062903 (2017).
- [53] K. To, Y.-K. Mo, T. Pongó, and T. Börzsönyi, Discharge of elongated grains from silo with rotating bottom, *Phys. Rev. E* **103**, 062905 (2021).